Supporting Information for

Machine learning guided tuning charge distribution by composition in MOFs for oxygen evolution reaction

Licheng Yu,[a] Wenwen Zhang,[a] Zhihao Nie,[a] Jingjing Duan[a] and Sheng Chen*[a]

[a]Key Laboratory for Soft Chemistry and Functional Materials (Ministry of Education), School of Chemistry and Chemical Engineering, School of Energy and Power Engineering, Nanjing University of Science and Technology, Nanjing, 210094, China

Correspondence and requests for materials should be addressed to: sheng.chen@njust.edu.cn

S1. Experimental Section

1.1 Chemicals

Copper acetate (Cu(CH$_3$COO)$_2$·H$_2$O, 99%), iron nitrate (Fe(NO$_3$)$_3$·9H$_2$O, 98%), zinc acetate (Zn(CH$_3$COO)$_2$·2H$_2$O, 99%), manganese acetate ((CH$_3$COO)$_2$Mn·4H$_2$O, 99%), cadmium acetate ((CH$_3$CO$_2$)$_2$Cd·xH$_2$O, 99%), Trimesic acid (C$_9$H$_6$O$_6$, 99%), potassium hydroxide (KOH, 99%), hydrochloric acid (HCl, 36%), were purchased from Sigma-Aldrich and directly used without further treatment or purification. All aqueous solutions were prepared with high-purity de-ionized water (DI-water, resistance 18.25 MΩ cm^{-1}).

1.2 Synthesis of MOFs

In a typical synthesis program, the mixed solution is made from 10 mL of solvent (composed of water and ethanol in ratios of 0:5, 1:4, 2:3, 3:2, 4:1, and 5:0, respectively) and 80 mg of metal salts. Next, add 100 mg of organic ligands to the above solution and seal the vial for reaction at 65 °C for t hours (t=23, 26, 29, 32, and 35 hours). After cooling to room temperature, the reaction products were taken out and centrifuged three times with deionized water, ethanol, and deionized water, respectively. The solid substances obtained were frozen with liquid nitrogen and moisture was removed in a vacuum dryer.

1.3 Working electrode preparation based on MOF for OER

1 mg of MOF, 1 mg of acetylene black, 30 μL of Nafion solution (5 wt%) were dispersed in 750 μL of isopropanol and 220 μL of water by ultrasonication for 1 h to form a homogeneous ink. Then, the dispersion was evenly dropped on the hydrophobic carbon paper with area of 1.0 cm^{-2} and loading level of 3.0 mg cm^{-2}, followed by dry under ambient conditions.

1.4 Physical characterizations

XRD was performed on a Philips 1130 X-ray diffractometer (40 kV, 25 mA, Cu Kα radiation, λ=1.5418 Å); Zeta potential was monitored on a Malvern ZS90 Zeta sizer Nano series analyzer; morphologies of the samples were observed on SEM (QUANTA 450);

1.5 Electrochemical characterizations

OER test was studied in a standard three-electrode glass cell connected to a 760E workstation (Pine Research Instruments, US) using the NiFe-MOF as the working electrode, carbon rod as a counter electrode, and Hg/HgO/KOH (1 M) as a reference electrode. All the measured potentials were converted to reversible hydrogen electrodes (RHE) according to Potential = $E_{Hg/HgO}$ + 0.059 pH + 0.098. The electrolyte was prepared using DI-water (18.25 MΩ cm^{-1}) and KOH. LSV and CV plots were recorded with the scan rates of 5 mV s^{-1} and 10 mV s^{-1}, respectively; Tafel plots were recorded with the linear portions at low overpotential fitted to the Tafel equation (η =

$b \log j + a$, where η is overpotential, j is the current density, and b is the Tafel slope);

EIS was recorded under the following conditions: AC voltage amplitude 0 or 1.5V,

frequency ranges 10^6 to 0.01 Hz, and open circuit; the current density was normalized

to the geometrical area; All CV and LSV data was presented without *iR* correction.

The electrochemical specific surface areas (ECSAs) of MOF nanosheets

electrodes were measured by cyclic voltammetry (CV) in the potential window of

1.228-1.328 V (*vs.* RHE) with different scan rates of 110, 130, 150, 170 and 190 mV

s^{-1} in 1 M KOH electrolyte. The plot of ΔJ (Ja- Jc, mA) at 1.25 V (*vs.* RHE) against

the scan rate was nearly linear, and its slope is twice the double layer capacitance (Cdl,

mF). We then used the benchmark specific capacitance of Cs = 0.035 mF cm^{-2} to

estimate the ECSAs of various electrodes (ECSA = Cdl/Cs).

1.6 Machine Learning Procedure

We used the Scikit-Learn package for the development of our ML models. To

evaluate the accuracy of zeta potential prediction, performance parameters such as

coefficient of determination (R^2), root mean square error (RMSE) and mean absolute

error (MAE) were calculated for the training and testing datasets. The root mean

square error (RMSE) is a statistical measure used to evaluate the generalization ability

of a model. It is calculated as the square root of the average square difference between

the predicted value of the target variable and the actual value. RMSE measures the

average difference between predicted and actual values and provides a concept of how much error the model generates in its prediction. A lower RMSE value indicates higher model accuracy, while a higher RMSE value indicates lower model accuracy. The mean absolute error (MAE) is another important statistical measure for evaluating model quality. If the MAE of a model is small or close to zero, it is considered effective and accurate.

$$\text{MAE} = \frac{1}{N}\sum_{i=1}^{N}\left|y_{\text{predicted}} - y_{\text{actual}}\right|$$

$$\text{RMSE} = \sqrt{\frac{1}{N}\sum_{i=1}^{N}(y_{predicted} - y_{actual})^2}$$

$$R^2 = 1 - \frac{\sum_{i=1}^{N}(y_{predicted} - y_{actual})^2}{\sum_{i=1}^{N}(y_{actual} - \bar{y})^2}$$

S2. Zeta potential curves of various MOF materials
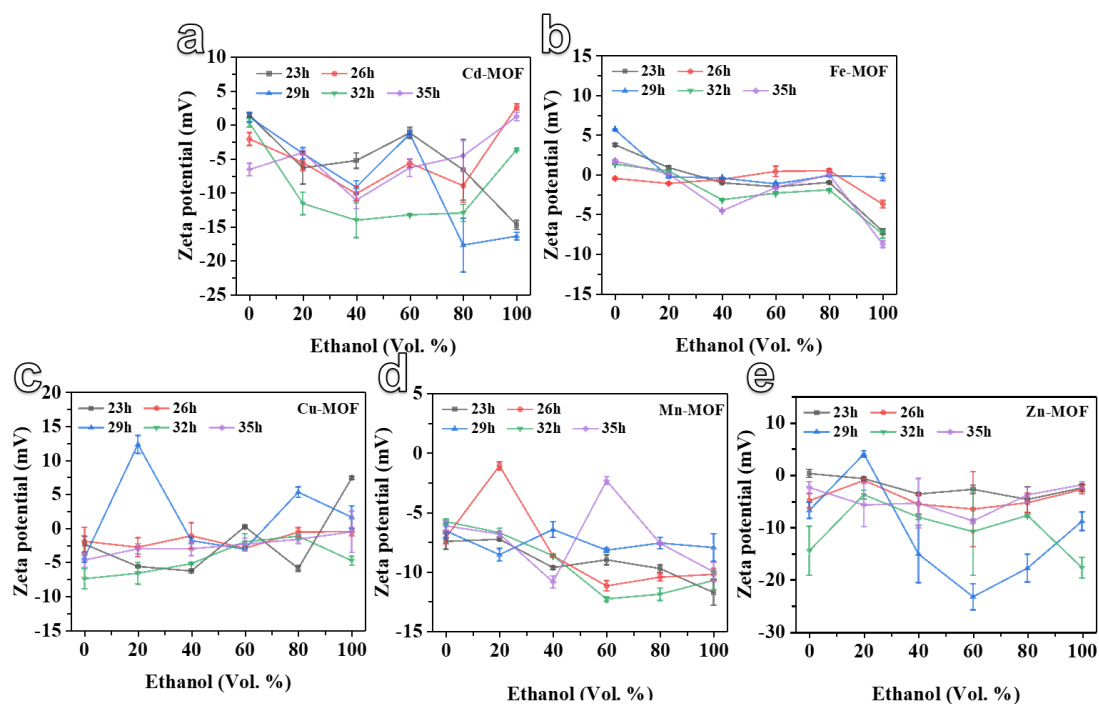
Figure S1. Zeta potential trend of MOFs synthesized at different temperatures and solvent ratios, (a-e) are Cd-MOF, Fe-MOF, Cu-MOF, Mn-MOF and Zn-MOF, respectively.
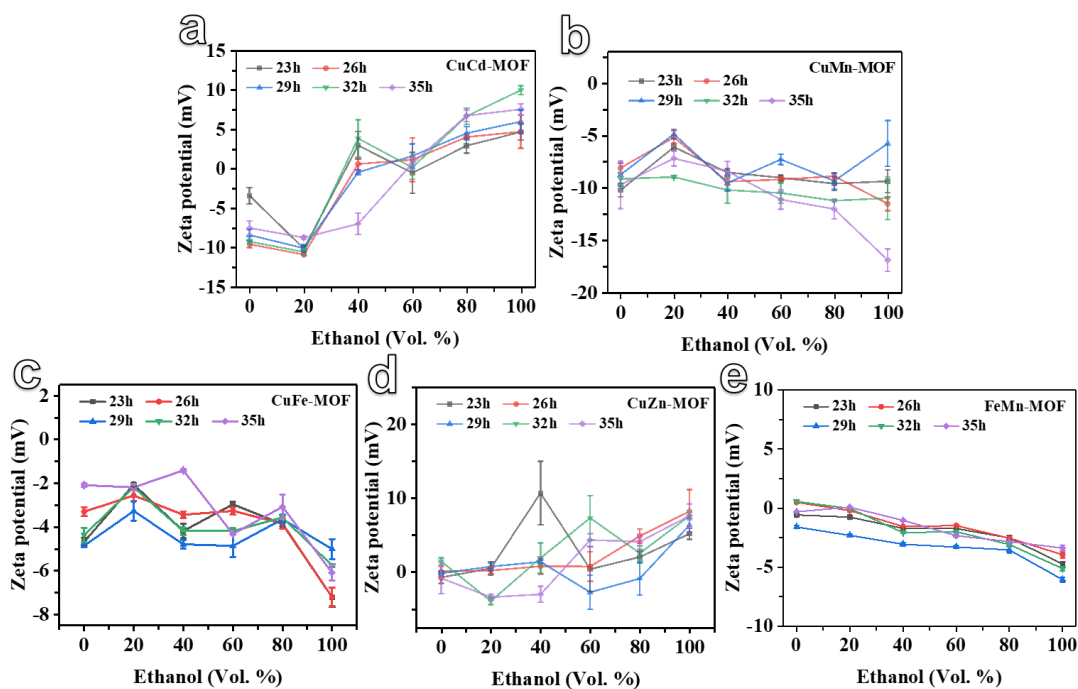
Figure S2. Zeta potential trend of MOFs synthesized at different temperatures and solvent ratios, (a-e) are CuCd-MOF, CuMn-MOF, CuFe-MOF, CuZn-MOF and FeMn-MOF, respectively.
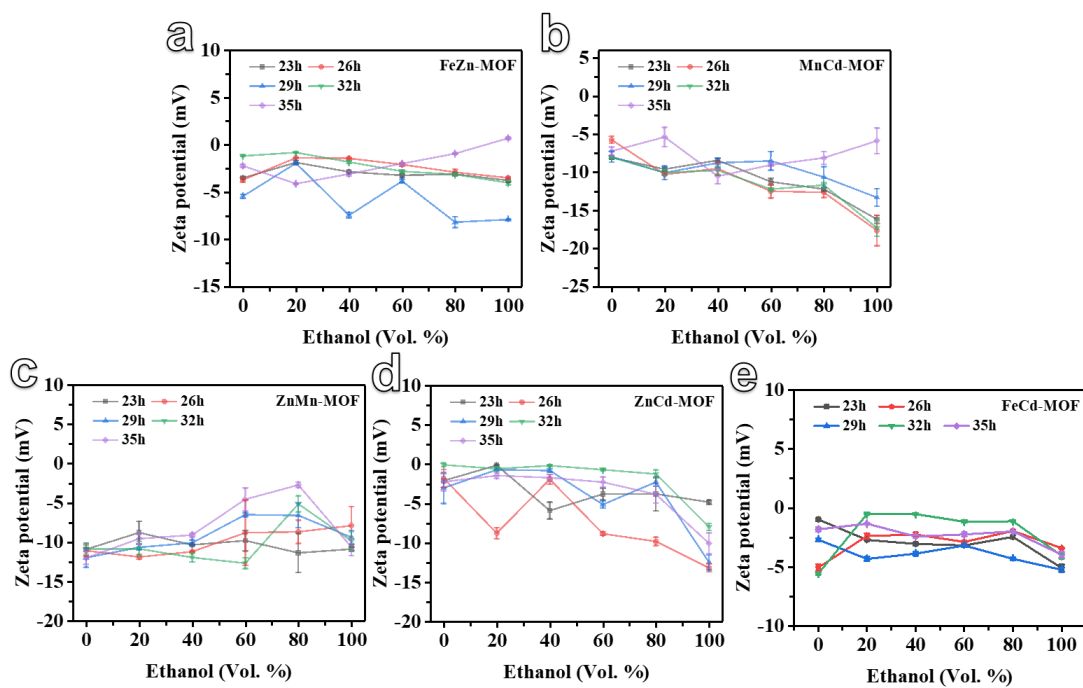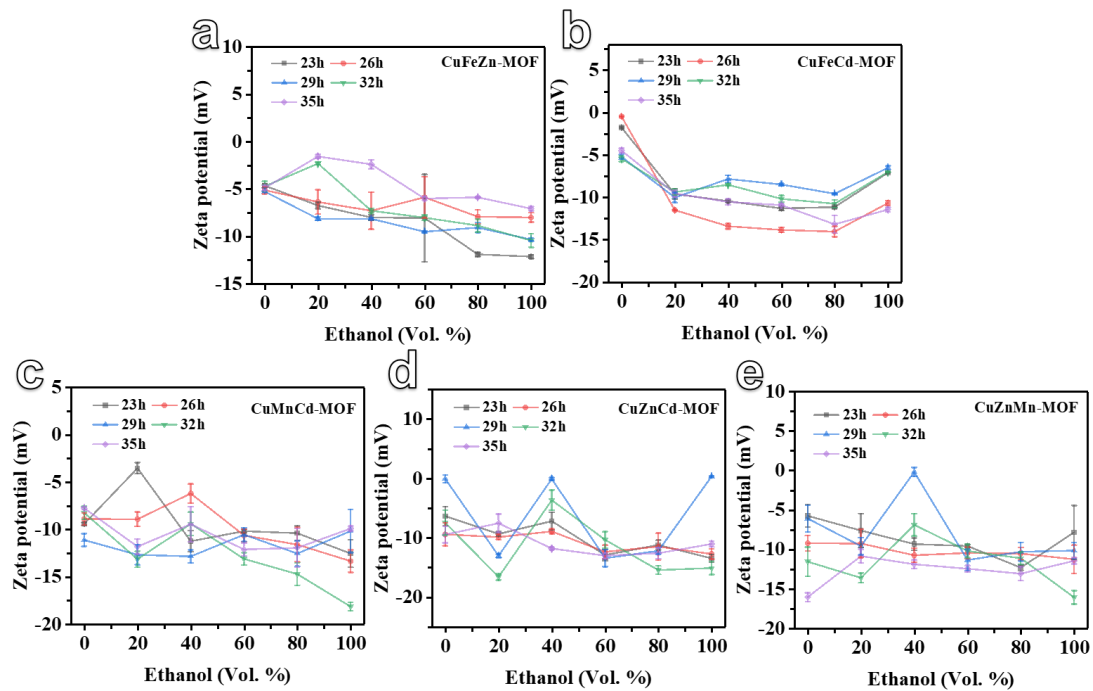
Figure S3. Zeta potential trend of MOFs synthesized at different temperatures and solvent ratios, (a-e) are FeZn-MOF, MnCd-MOF, ZnMn-MOF, ZnCd-MOF and FeCd-MOF, respectively.

Figure S4. Zeta potential trend of MOFs synthesized at different temperatures and solvent ratios, (a-e) are CuFeZn-MOF, CuFeCd-MOF, CuMnCd-MOF, CuZnCd-MOF and CuZnMn-MOF, respectively.
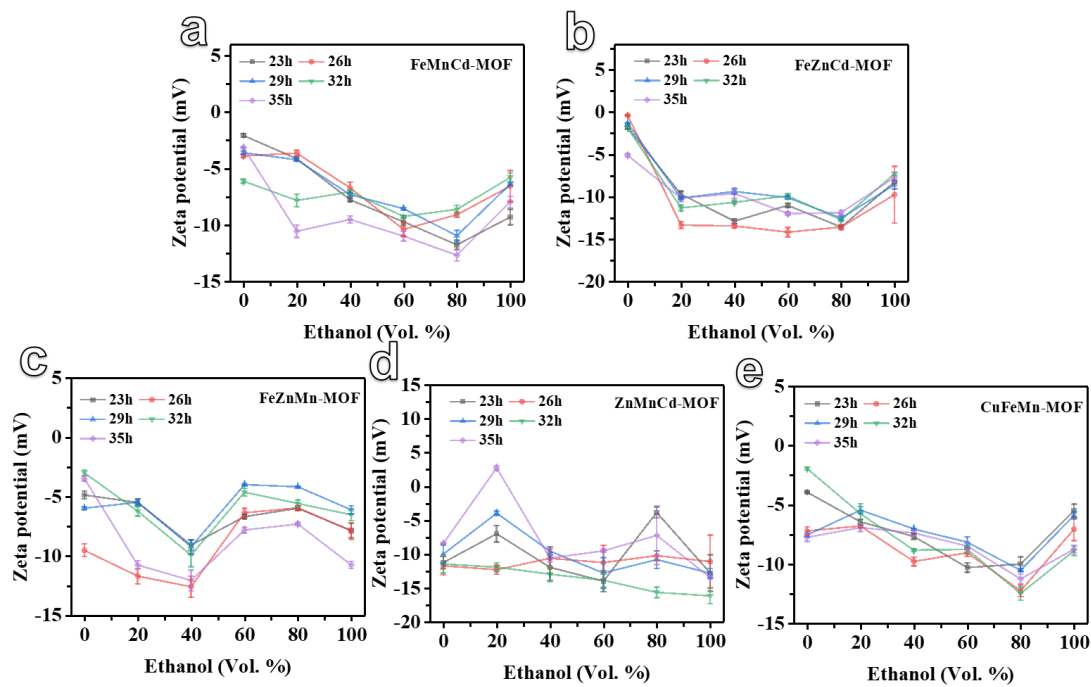
Figure S5. Zeta potential trend of MOFs synthesized at different temperatures and solvent ratios, (a-e) are FeMnCd-MOF, FeZnCd-MOF, FeZnMn-MOF, ZnMnCd-MOF and CuFeMn-MOF, respectively.
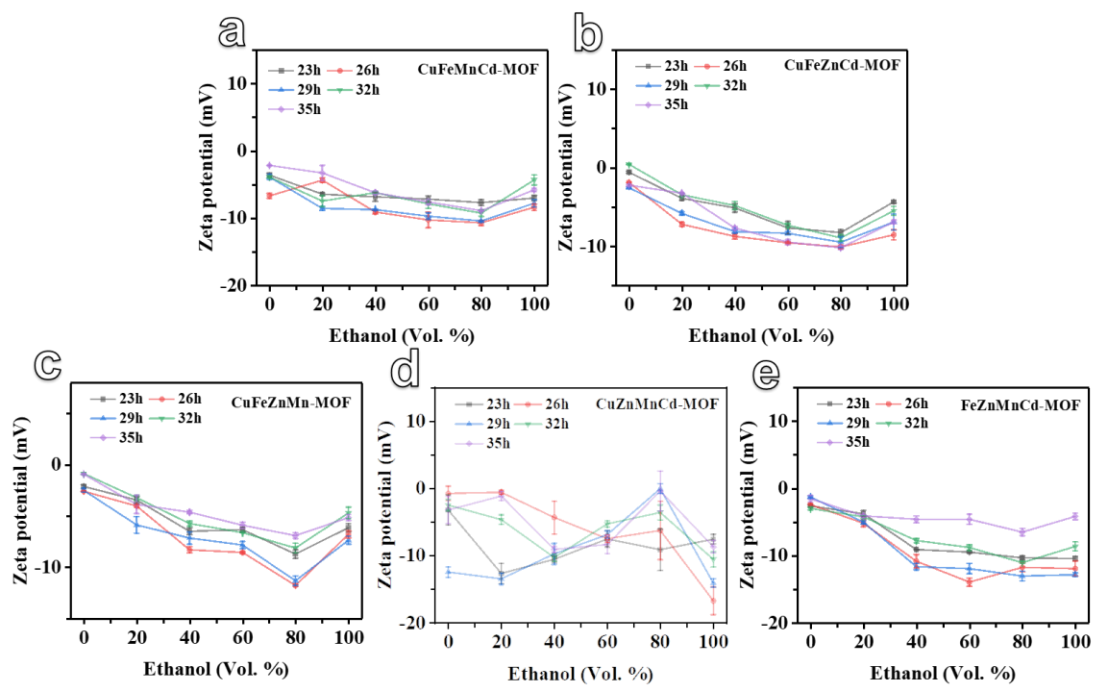
Figure S6. Zeta potential trend of MOFs synthesized at different temperatures and solvent ratios, (a-e) are CuFeMnCd-MOF, CuFeZnCd-MOF, CuFeZnMn-MOF, CuZnMnCd-MOF and FeZnMCd-MOF, respectively.

Table S1. Parameter list of four regression methods for machine learning models.

Method	Tuning parameters [tested range]
RFR	n_estimators = [100, 250, 500]
GBR	Learning_rate = [1.0, 10^{-1}, 10^{-2}, 10^{-3}, 10^{-4}, 10^{-5}] Max_depth = [4, 6, 8, 10] n_estimators = [100, 250, 500]
SVM	kernel = 'rbf' C = 250 gamma = 1
KNN	n_neighbours = [4, 6, 8, 10]

S3. ML fitting diagram of the dataset.
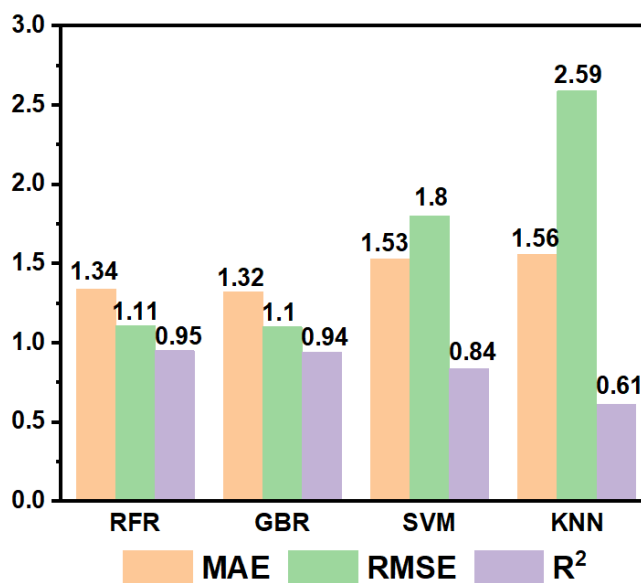
Figure S7. The mean absolute error (MAE), root mean square error (RMSE) and R^2 of four machine learning training models, namely k- near neighbor (KNN), gradient lifting regression (GBR), random forest regression (RFR), and support vector machine (SVM).
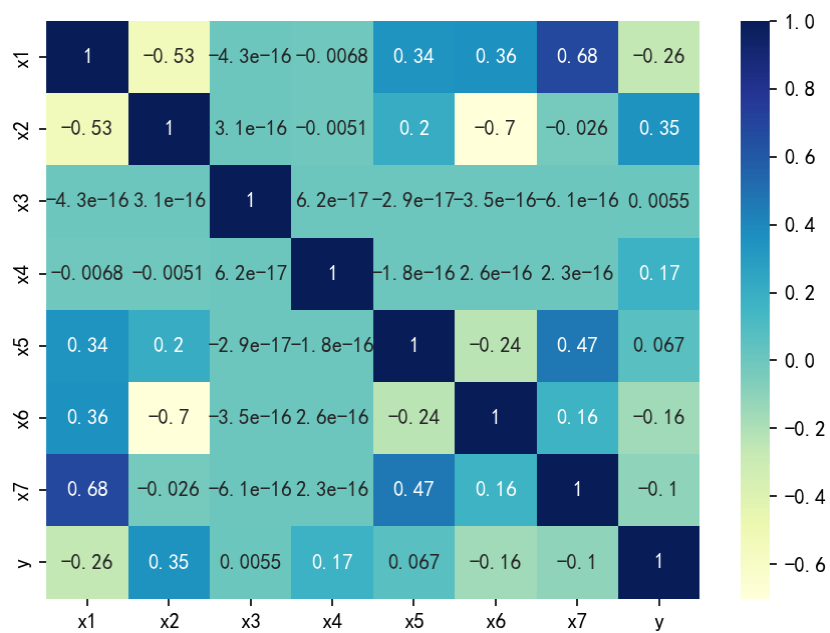
Figure S8. Thermodynamic correlation diagrams of various parameters, x1. x2, x3, x4, x5, x6, x7, and y represent atomic radius, electronegativity, time, proportion, main group number, outermost electron number, atomic number, and zeta potential, respectively.
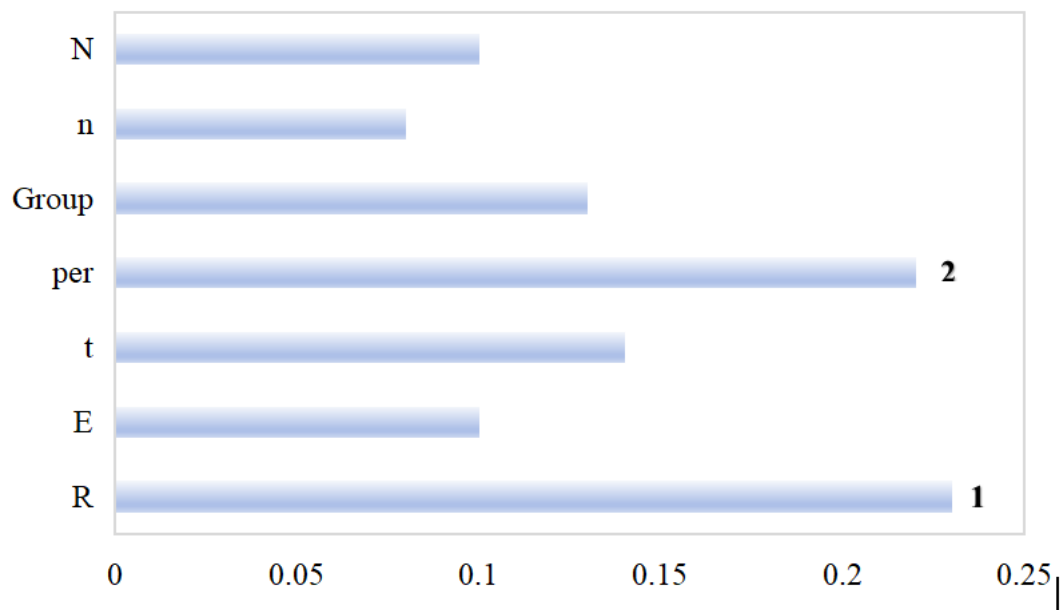
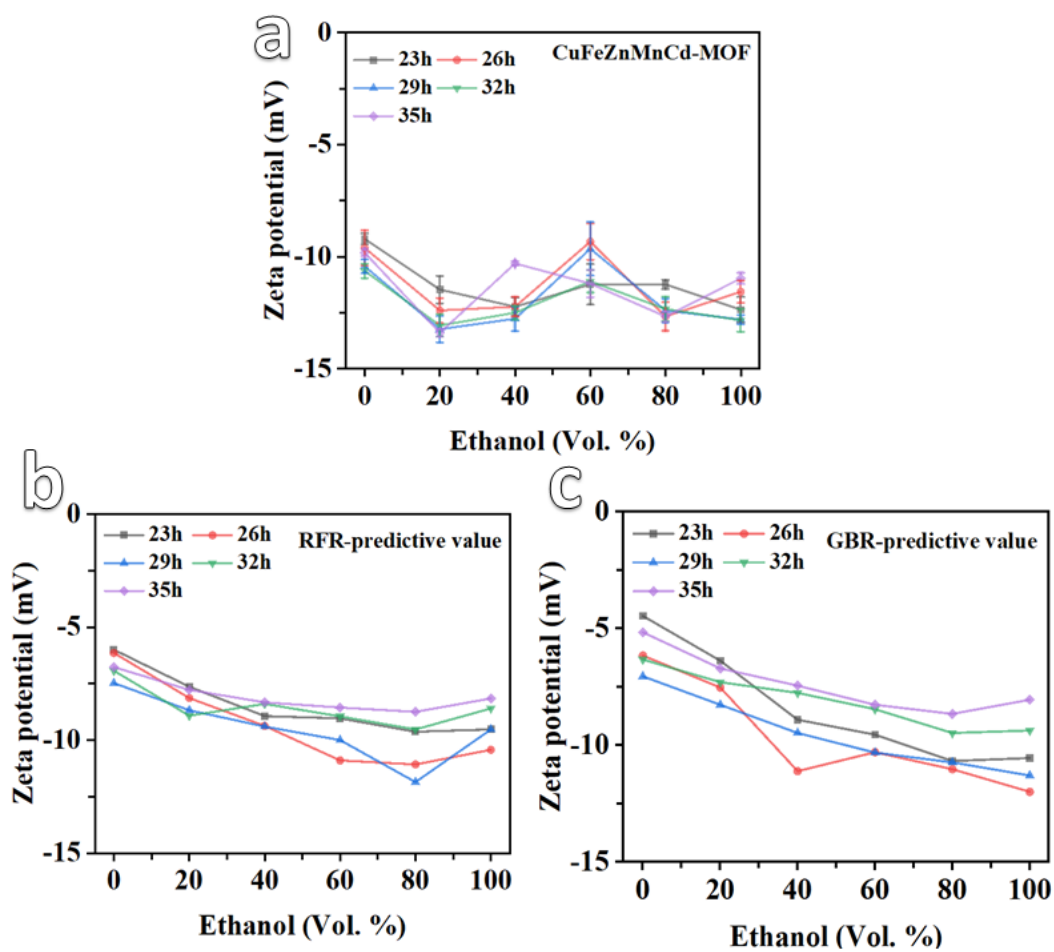**Figure S9.** Importance score graph of feature descriptors.

Figure S10. Zeta potential trend of MOFs synthesized at different temperatures and solvent ratios; (a) represents the experimental test value, while (b) and (c) represent the predicted values of the RFR and GBR models, respectively.

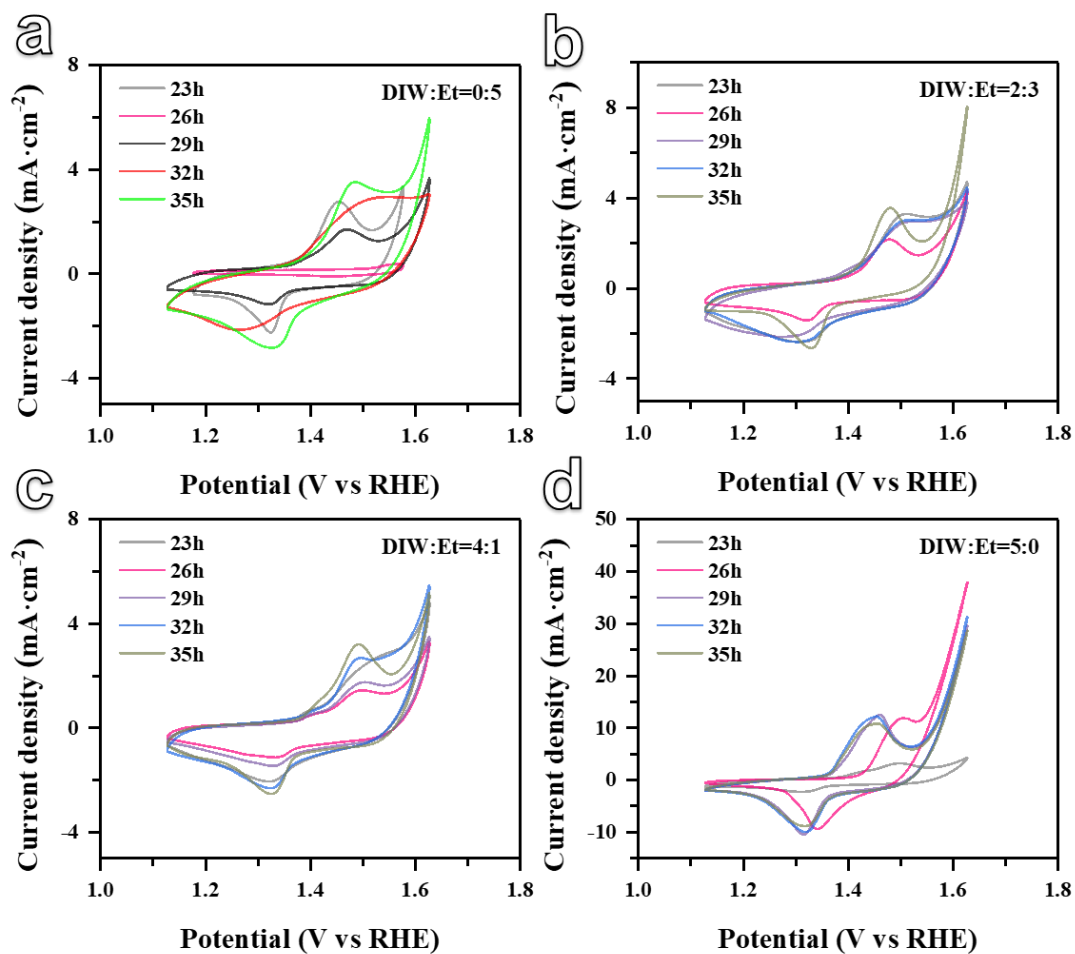**S4. Electrochemical performance diagram of five metal MOFs.**

Figure S11. Electrochemical cyclic voltammetry (CV) curves of MOFs synthesized

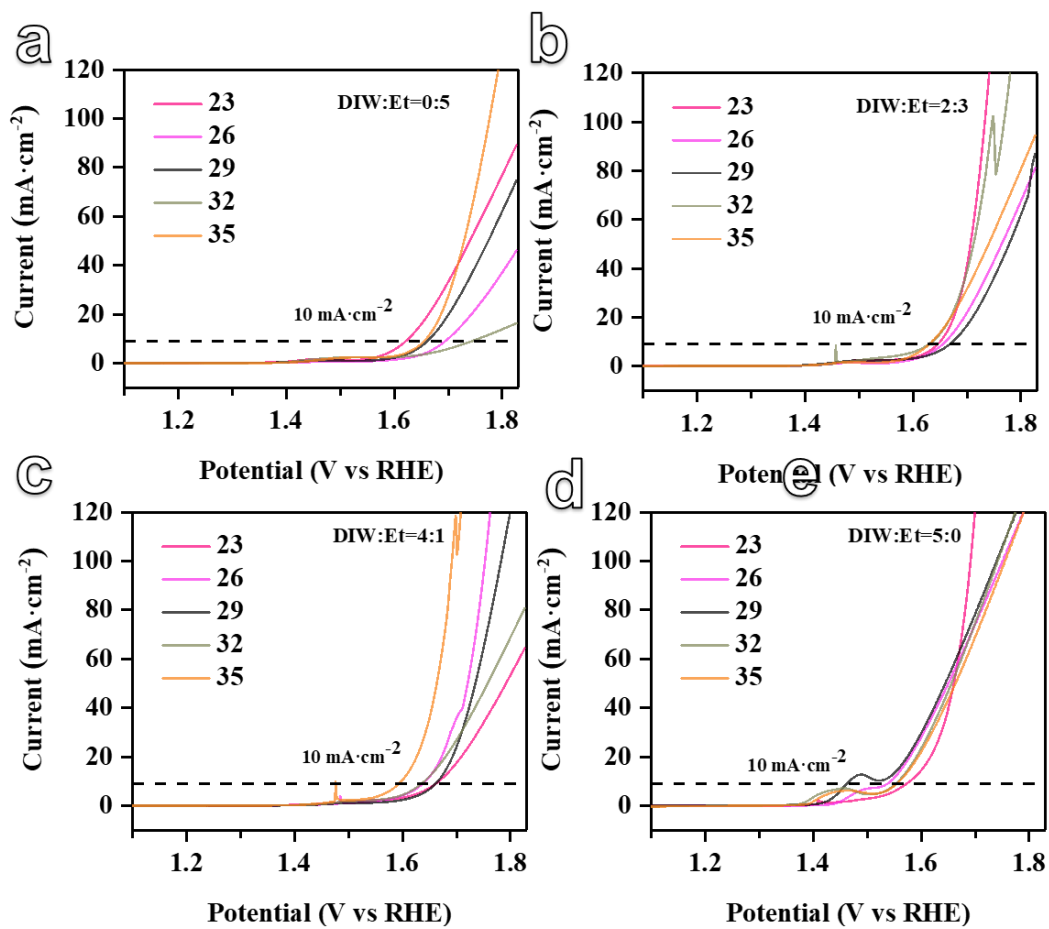with different solvent ratios and reaction temperatures.

Figure S12. Linear sweep voltammetry (LSV) curves of MOF synthesized with different solvent ratios and reaction temperatures, current density relative to applied potential.
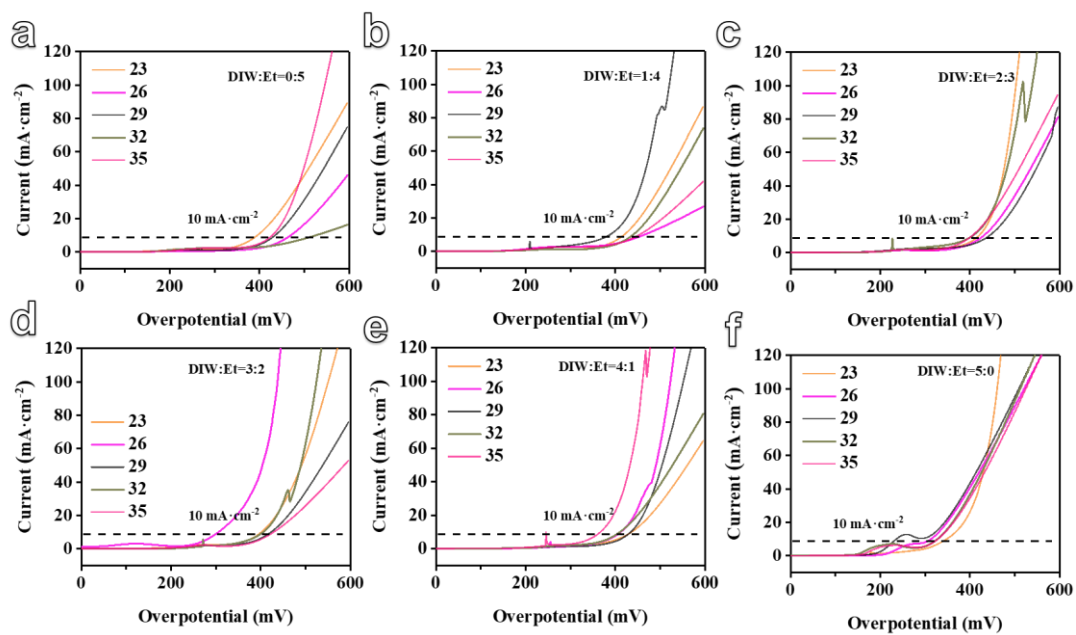
Figure S13. Linear sweep voltammetry (LSV) curves of MOF synthesized with different solvent ratios and reaction temperatures, current density relative to applied overpotential.
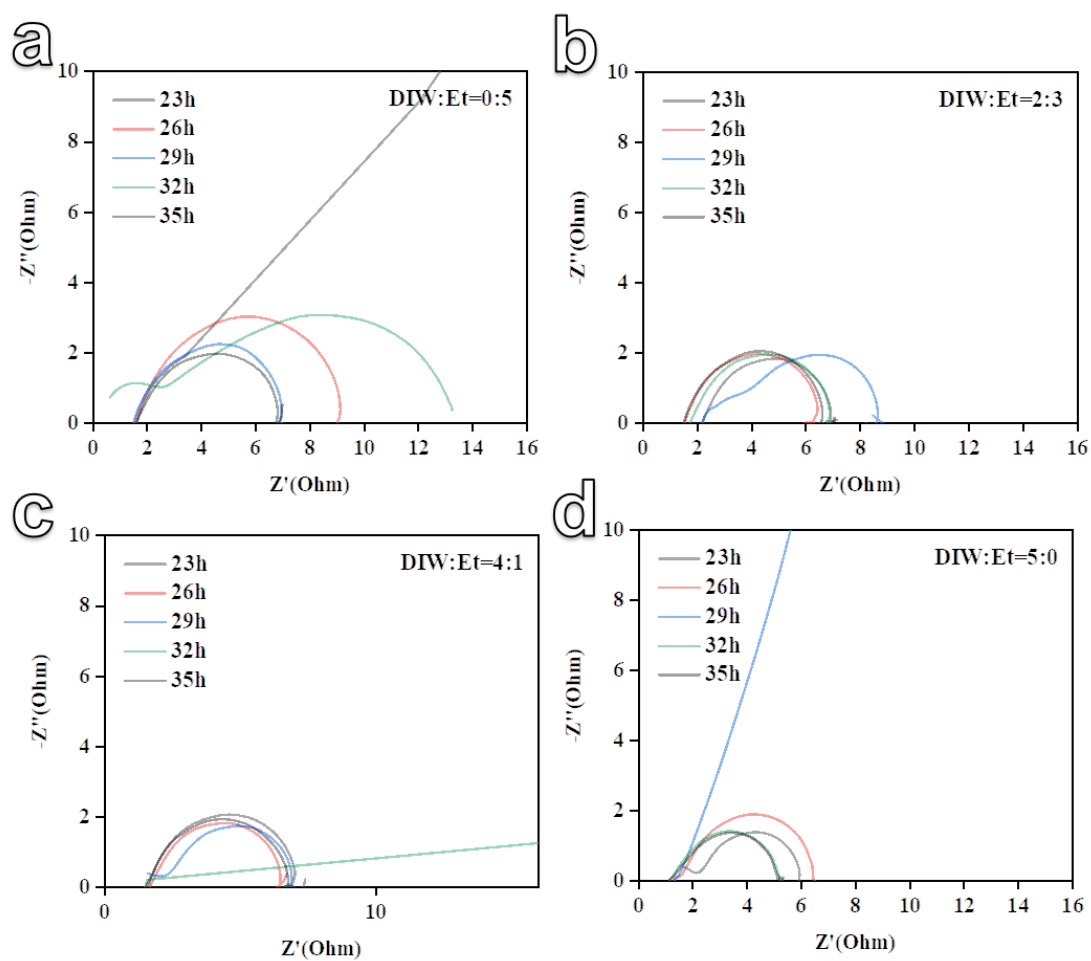
Figure S14. EIS spectra of MOF synthesized with different solvent ratios and reaction temperatures.
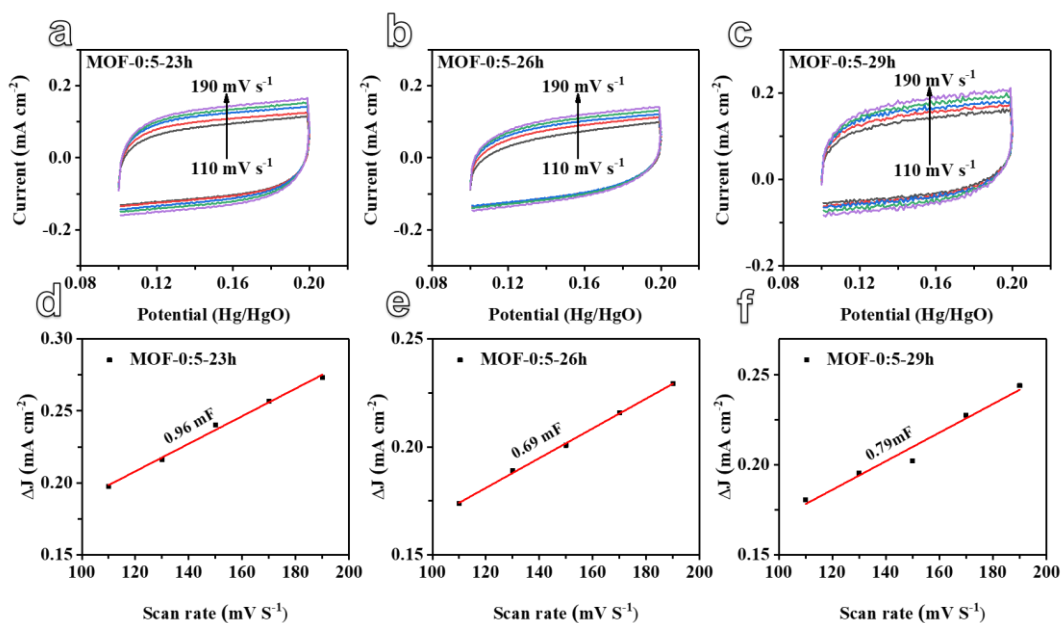
Figure S15. Capacitance studies on MOF samples synthesized at different temperatures in a solvent ratio of DIW: Et = 0: 5, (a-c) are 23 h, 26 h, and 29 h, respectively. The corresponding CVs measured at different scan rates from 110 to 190 mV s^{-1} in a potential region of 0.1 ~ 0.2 V (Hg/HgO). The C_{dl} value of the synthesized electrode was evaluated on the basis of CVs. The CVs of both samples exhibit a typical rectangular shape of an electrical double layer capacitor. In this potential region, the charge transfer electrode reactions are considered to be negligible and the current originates solely from electrical double layer charging and discharging. The plot of current density (at 0.15 V *vs*. Hg/HgO) against scan rate has a linear relationship, and its slope is the double layer capacitance.
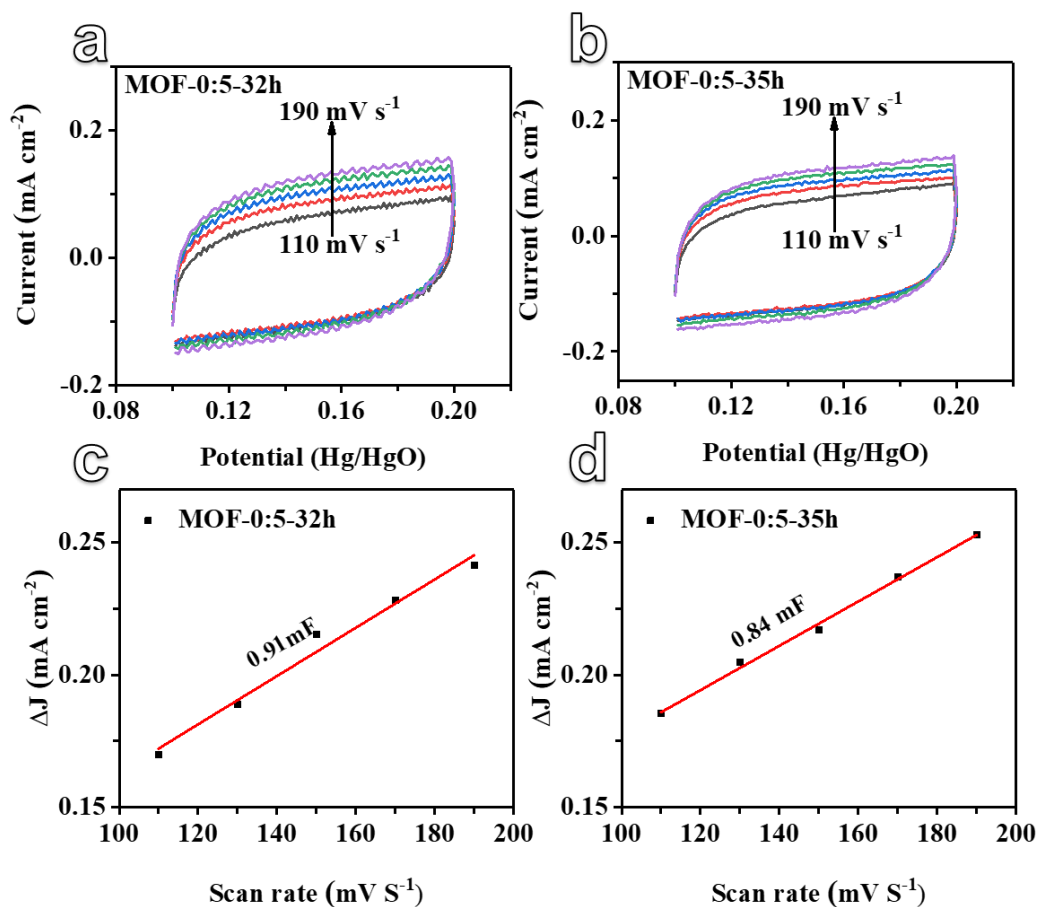
Figure S16. Capacitance studies on MOF samples synthesized at different temperatures in a solvent ratio of DIW: Et = 0: 5, (a, b) are 32 h and 35 h, respectively. The corresponding CVs measured at different scan rates from 110 to 190 mV s^{-1} in a potential region of 0.1 ~ 0.2 V (Hg/HgO). The C$_{dl}$ value of the synthesized electrode was evaluated on the basis of CVs. The CVs of both samples exhibit a typical rectangular shape of an electrical double layer capacitor. In this potential region, the charge transfer electrode reactions are considered to be negligible and the current originates solely from electrical double layer charging and discharging. The plot of current density (at 0.15 V *vs.* Hg/HgO) against scan rate has a linear relationship, and its slope is the double layer capacitance.
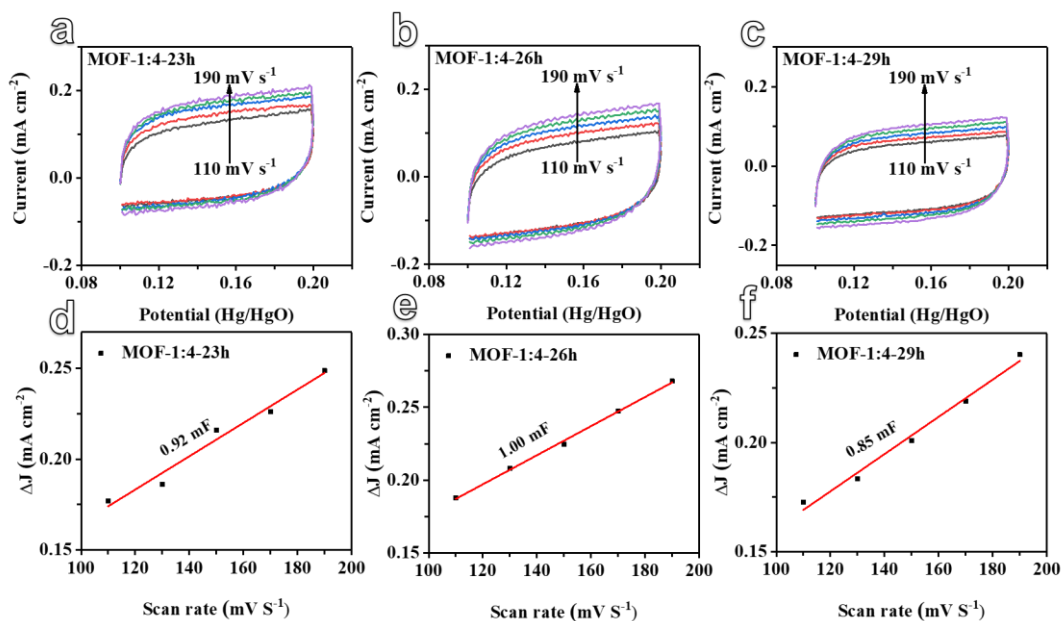
Figure S17. Capacitance studies on MOF samples synthesized at different temperatures in a solvent ratio of DIW: Et = 1: 4, (a, b) are 23 h, 26 h and 29 h, respectively. The corresponding CVs measured at different scan rates from 110 to 190 mV s^{-1} in a potential region of 0.1 ~ 0.2 V (Hg/HgO). The C_{dl} value of the synthesized electrode was evaluated on the basis of CVs. The CVs of both samples exhibit a typical rectangular shape of an electrical double layer capacitor. In this potential region, the charge transfer electrode reactions are considered to be negligible and the current originates solely from electrical double layer charging and discharging. The plot of current density (at 0.15 V *vs.* Hg/HgO) against scan rate has a linear relationship, and its slope is the double layer capacitance.
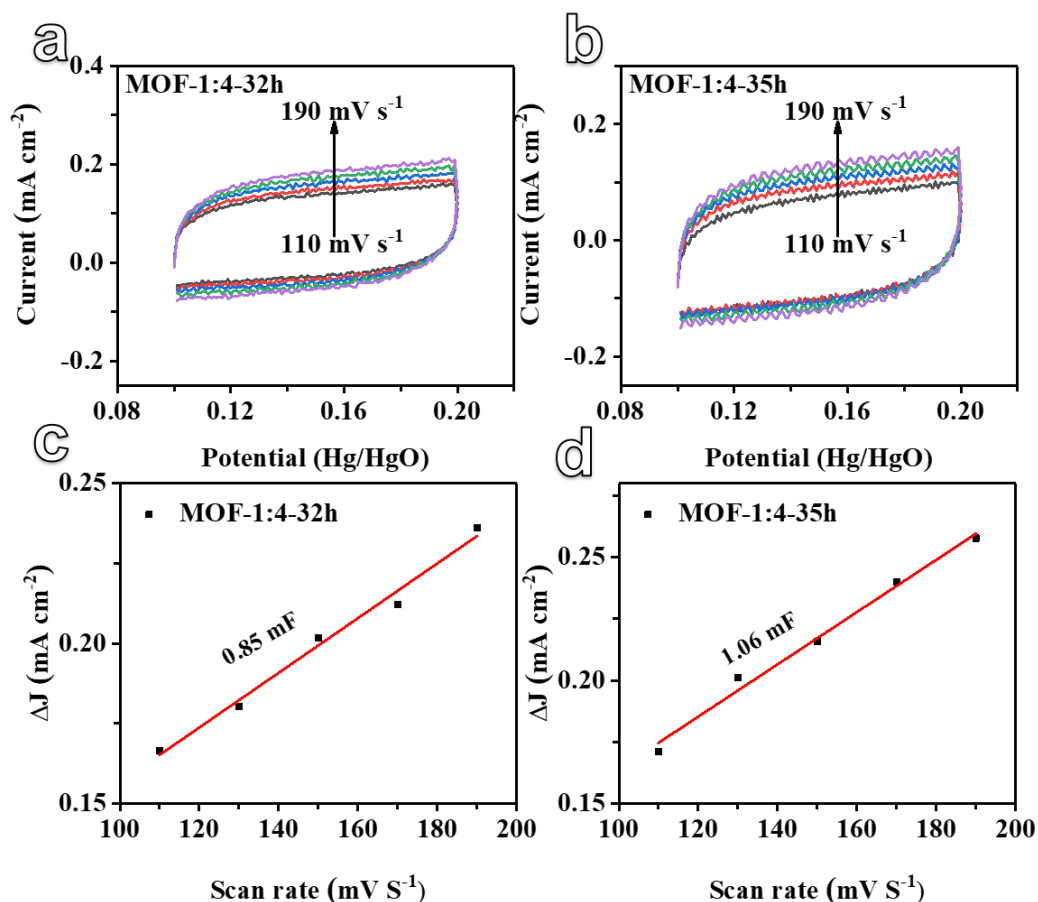
Figure S18. Capacitance studies on MOF samples synthesized at different temperatures in a solvent ratio of DIW: Et = 1: 4, (a, b) are 32 h and 35 h, respectively. The corresponding CVs measured at different scan rates from 110 to 190 mV s^{-1} in a potential region of 0.1 ~ 0.2 V (Hg/HgO). The C$_{dl}$ value of the synthesized electrode was evaluated on the basis of CVs. The CVs of both samples exhibit a typical rectangular shape of an electrical double layer capacitor. In this potential region, the charge transfer electrode reactions are considered to be negligible and the current originates solely from electrical double layer charging and discharging. The plot of current density (at 0.15 V *vs.* Hg/HgO) against scan rate has a linear relationship, and its slope is the double layer capacitance.
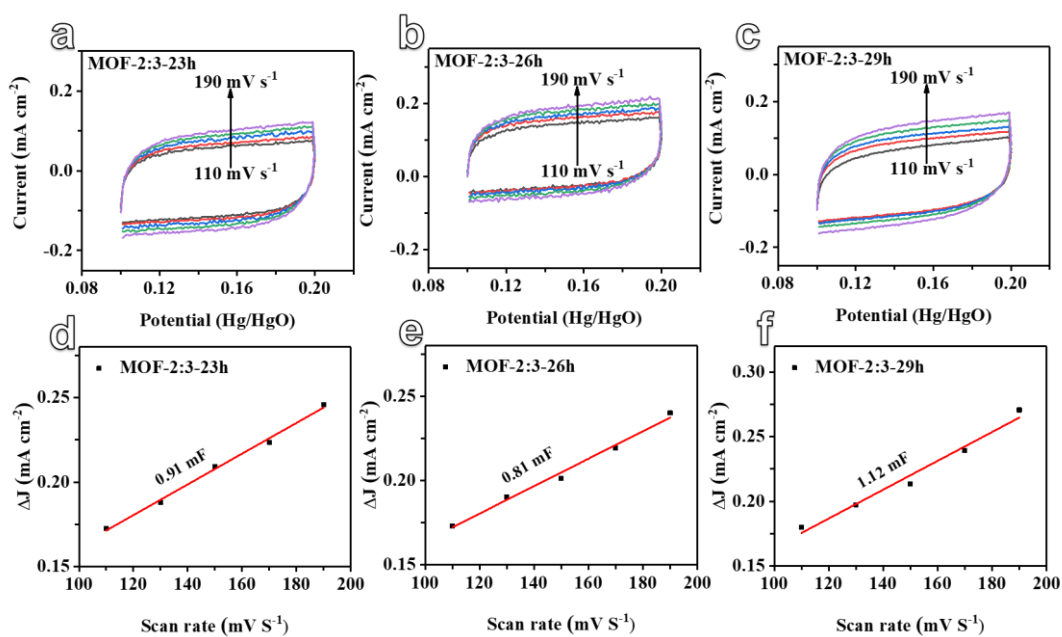
Figure S19. Capacitance studies on MOF samples synthesized at different temperatures in a solvent ratio of DIW: Et = 2: 3, (a, b) are 23 h, 26 h and 29 h, respectively. The corresponding CVs measured at different scan rates from 110 to 190 mV s^{-1} in a potential region of 0.1 ~ 0.2 V (Hg/HgO). The C_{dl} value of the synthesized electrode was evaluated on the basis of CVs. The CVs of both samples exhibit a typical rectangular shape of an electrical double layer capacitor. In this potential region, the charge transfer electrode reactions are considered to be negligible and the current originates solely from electrical double layer charging and discharging. The plot of current density (at 0.15 V *vs.* Hg/HgO) against scan rate has a linear relationship, and its slope is the double layer capacitance.
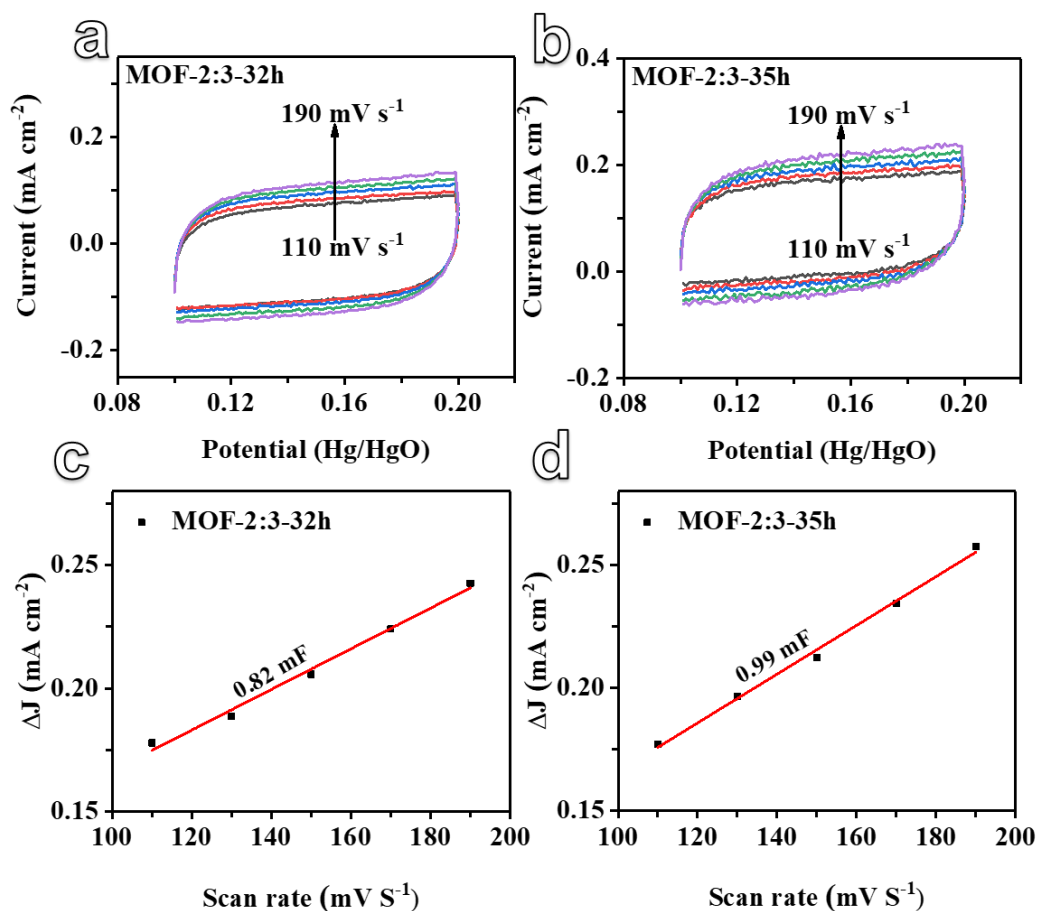
Figure S20. Capacitance studies on MOF samples synthesized at different temperatures in a solvent ratio of DIW: Et = 2: 3, (a, b) are 32 h and 35 h, respectively. The corresponding CVs measured at different scan rates from 110 to 190 mV s^{-1} in a potential region of 0.1 ~ 0.2 V (Hg/HgO). The C_{dl} value of the synthesized electrode was evaluated on the basis of CVs. The CVs of both samples exhibit a typical rectangular shape of an electrical double layer capacitor. In this potential region, the charge transfer electrode reactions are considered to be negligible and the current originates solely from electrical double layer charging and discharging. The plot of current density (at 0.15 V *vs.* Hg/HgO) against scan rate has a linear relationship, and its slope is the double layer capacitance.
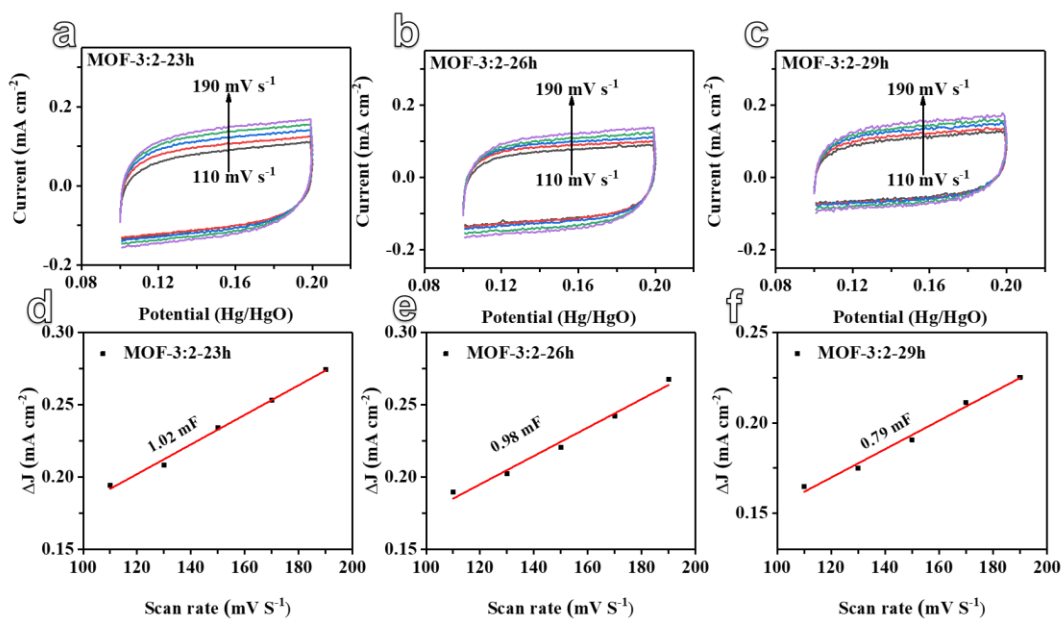
Figure S21. Capacitance studies on MOF samples synthesized at different temperatures in a solvent ratio of DIW: Et = 3: 2, (a, b) are 23 h, 26 h and 29 h, respectively. The corresponding CVs measured at different scan rates from 110 to 190 mV s^{-1} in a potential region of 0.1 ~ 0.2 V (Hg/HgO). The C_{dl} value of the synthesized electrode was evaluated on the basis of CVs. The CVs of both samples exhibit a typical rectangular shape of an electrical double layer capacitor. In this potential region, the charge transfer electrode reactions are considered to be negligible and the current originates solely from electrical double layer charging and discharging. The plot of current density (at 0.15 V *vs.* Hg/HgO) against scan rate has a linear relationship, and its slope is the double layer capacitance.
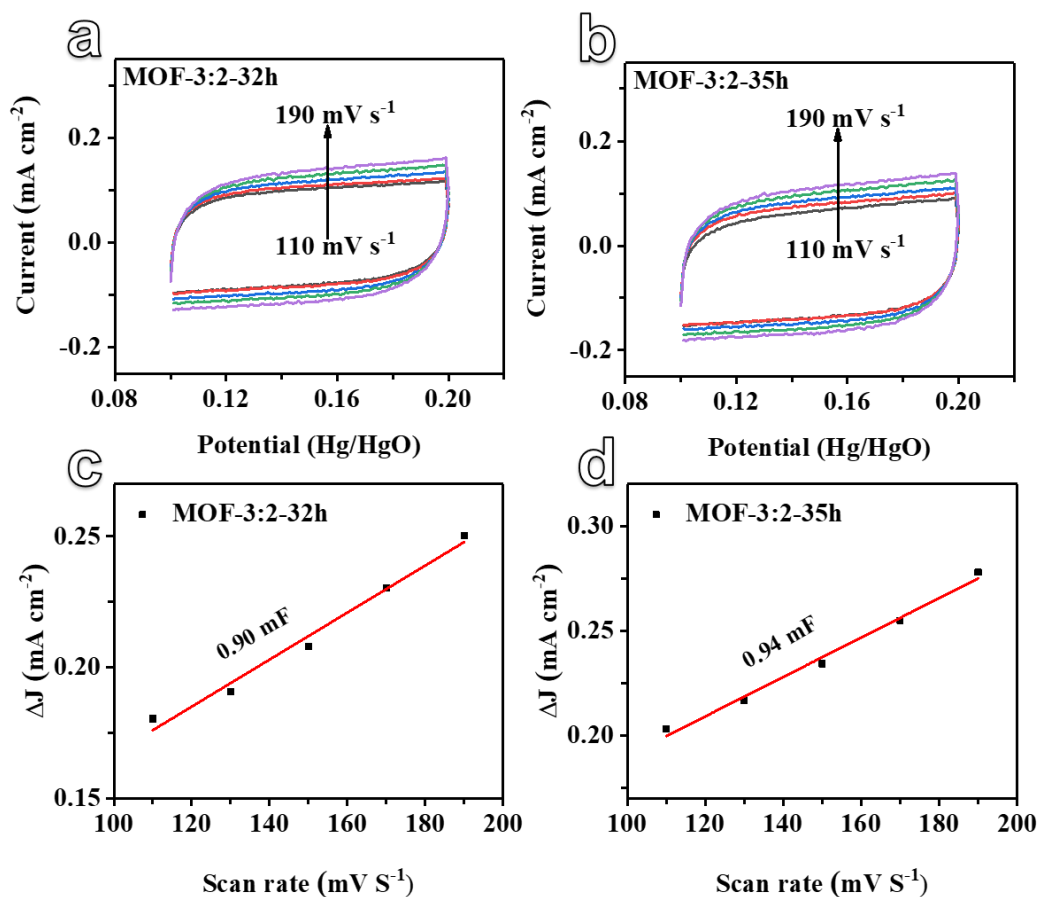
Figure S22. Capacitance studies on MOF samples synthesized at different temperatures in a solvent ratio of DIW: Et = 3: 2, (a, b) are 32 h and 35 h, respectively. The corresponding CVs measured at different scan rates from 110 to 190 mV s^{-1} in a potential region of 0.1 ~ 0.2 V (Hg/HgO). The C$_{dl}$ value of the synthesized electrode was evaluated on the basis of CVs. The CVs of both samples exhibit a typical rectangular shape of an electrical double layer capacitor. In this potential region, the charge transfer electrode reactions are considered to be negligible and the current originates solely from electrical double layer charging and discharging. The plot of current density (at 0.15 V *vs.* Hg/HgO) against scan rate has a linear relationship, and its slope is the double layer capacitance.
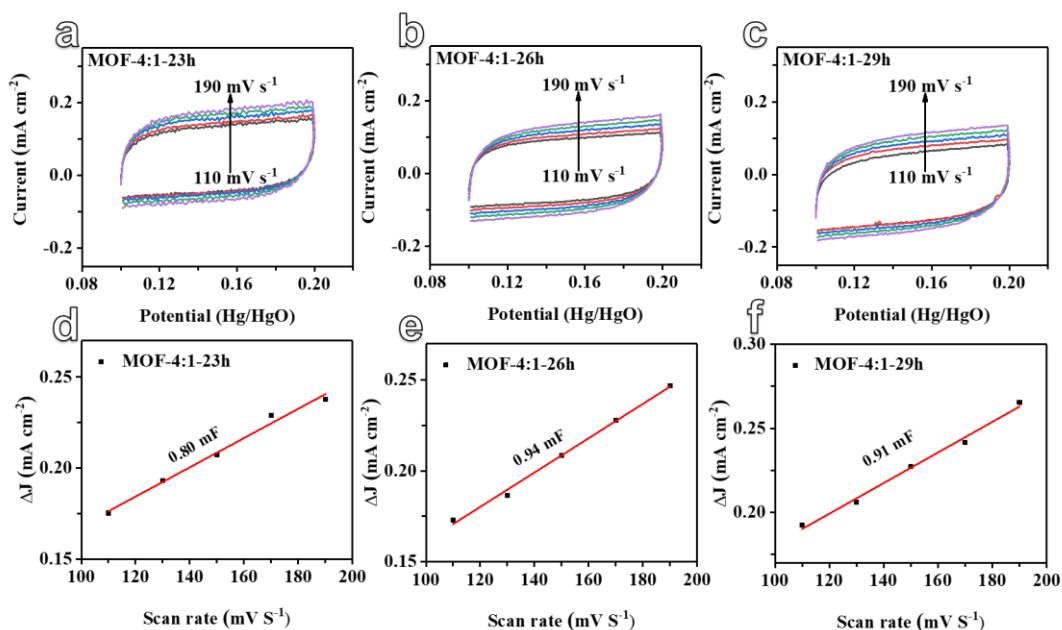
Figure S23. Capacitance studies on MOF samples synthesized at different temperatures in a solvent ratio of DIW: Et = 4: 1, (a, b) are 23 h, 26 h and 29 h, respectively. The corresponding CVs measured at different scan rates from 110 to 190 mV s^{-1} in a potential region of 0.1 ~ 0.2 V (Hg/HgO). The C_{dl} value of the synthesized electrode was evaluated on the basis of CVs. The CVs of both samples exhibit a typical rectangular shape of an electrical double layer capacitor. In this potential region, the charge transfer electrode reactions are considered to be negligible and the current originates solely from electrical double layer charging and discharging. The plot of current density (at 0.15 V *vs.* Hg/HgO) against scan rate has a linear relationship, and its slope is the double layer capacitance.
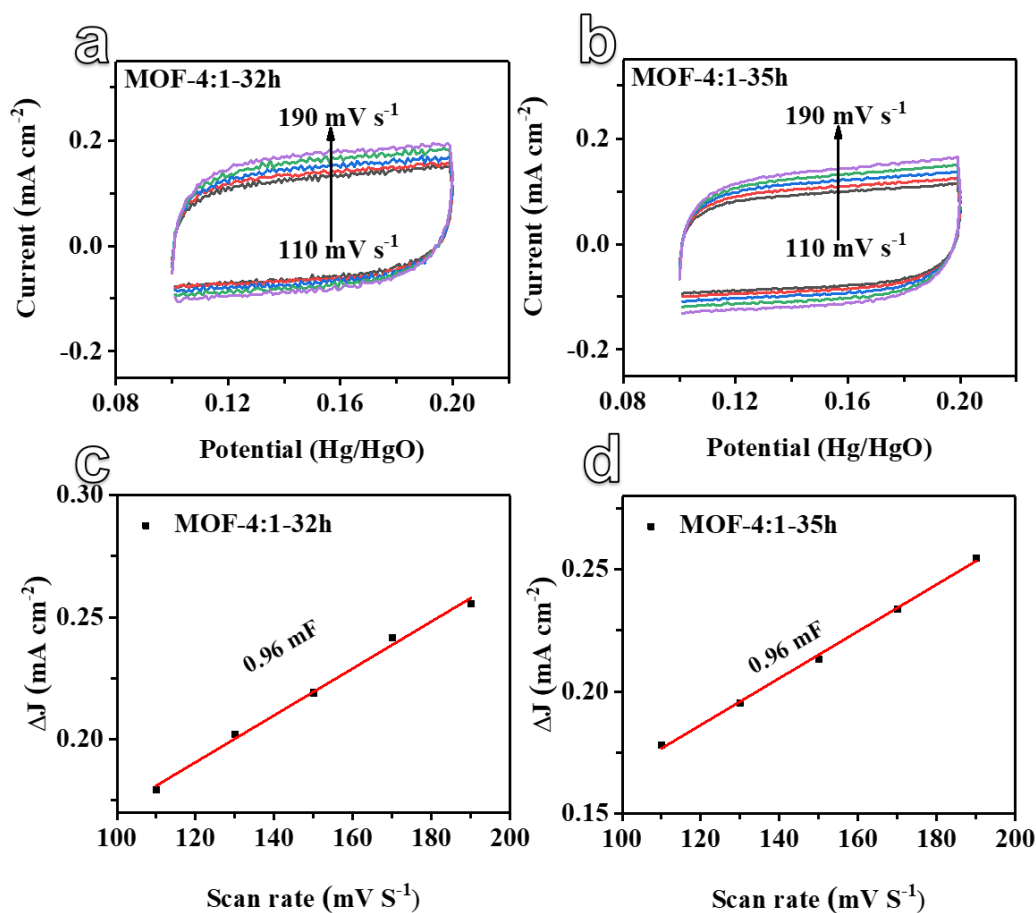
Figure S24. Capacitance studies on MOF samples synthesized at different temperatures in a solvent ratio of DIW: Et = 4: 1, (a, b) are 32 h and 35 h, respectively. The corresponding CVs measured at different scan rates from 110 to 190 mV s^{-1} in a potential region of 0.1 ~ 0.2 V (Hg/HgO). The C_{dl} value of the synthesized electrode was evaluated on the basis of CVs. The CVs of both samples exhibit a typical rectangular shape of an electrical double layer capacitor. In this potential region, the charge transfer electrode reactions are considered to be negligible and the current originates solely from electrical double layer charging and discharging. The plot of current density (at 0.15 V *vs.* Hg/HgO) against scan rate has a linear relationship, and its slope is the double layer capacitance.
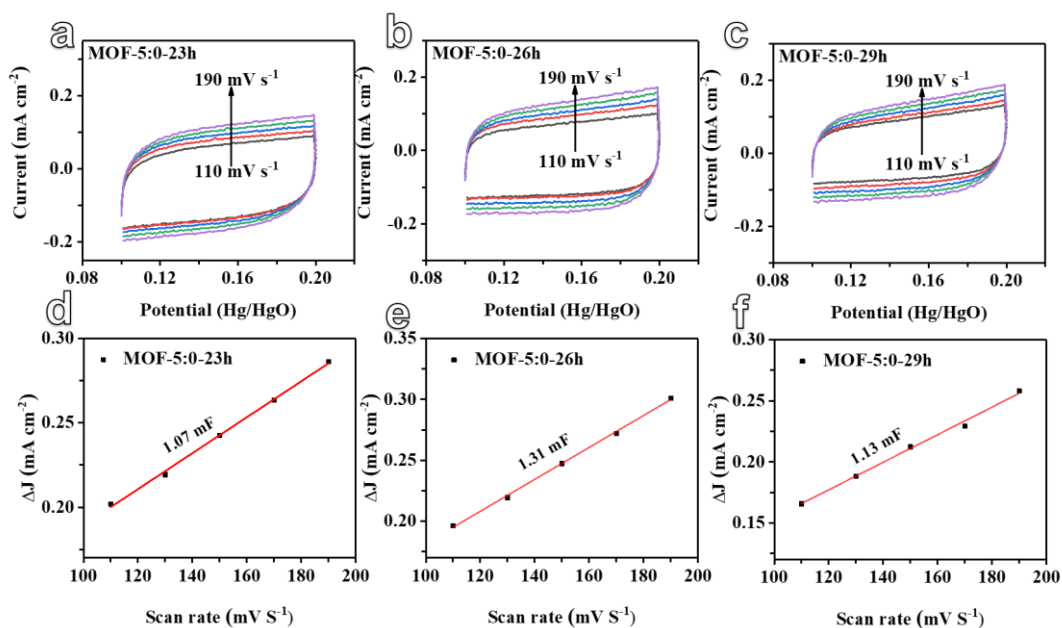
Figure S25. Capacitance studies on MOF samples synthesized at different temperatures in a solvent ratio of DIW: Et = 5: 0, (a, b) are 23 h, 26 h and 29 h, respectively. The corresponding CVs measured at different scan rates from 110 to 190 mV s^{-1} in a potential region of 0.1 ~ 0.2 V (Hg/HgO). The C_{dl} value of the synthesized electrode was evaluated on the basis of CVs. The CVs of both samples exhibit a typical rectangular shape of an electrical double layer capacitor. In this potential region, the charge transfer electrode reactions are considered to be negligible and the current originates solely from electrical double layer charging and discharging. The plot of current density (at 0.15 V *vs.* Hg/HgO) against scan rate has a linear relationship, and its slope is the double layer capacitance.
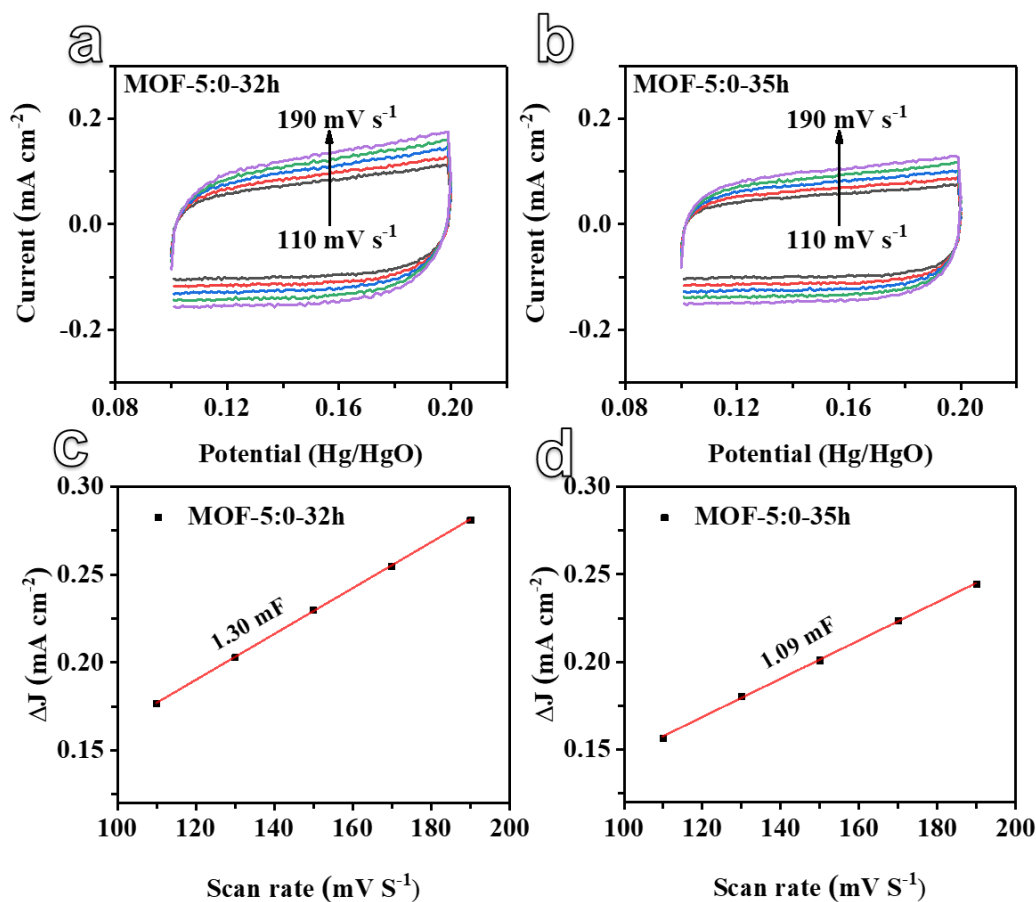
Figure S26. Capacitance studies on MOF samples synthesized at different temperatures in a solvent ratio of DIW: Et = 5: 0, (a, b) are 32 h and 35 h, respectively. The corresponding CVs measured at different scan rates from 110 to 190 mV s^{-1} in a potential region of 0.1 ~ 0.2 V (Hg/HgO). The C$_{dl}$ value of the synthesized electrode was evaluated on the basis of CVs. The CVs of both samples exhibit a typical rectangular shape of an electrical double layer capacitor. In this potential region, the charge transfer electrode reactions are considered to be negligible and the current originates solely from electrical double layer charging and discharging. The plot of current density (at 0.15 V *vs.* Hg/HgO) against scan rate has a linear relationship, and its slope is the double layer capacitance.
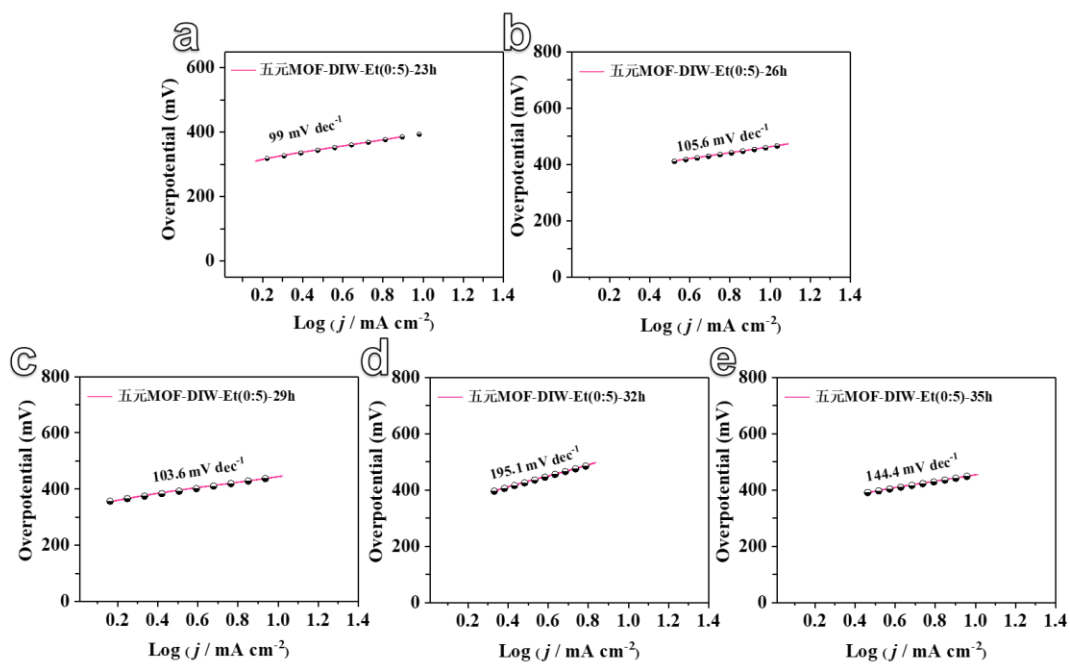
Figure S27. Tafel slope plots of MOFs synthesized at different temperatures in a solvent ratio of DIW: Et = 0: 5, (a-e) are 23 h, 26 h, 29 h, 32 h and 35 h, respectively.
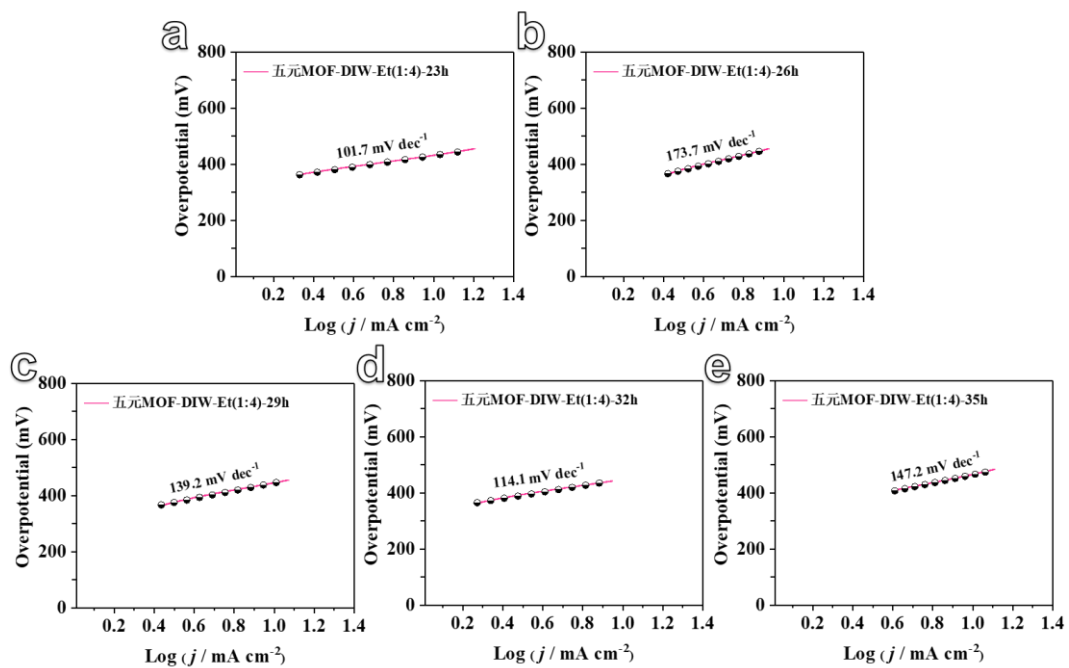
Figure S28. Tafel slope plots of MOFs synthesized at different temperatures in a solvent ratio of DIW: Et = 1: 4, (a-e) are 23 h, 26 h, 29 h, 32 h and 35 h, respectively.

Figure S29. Tafel slope plots of MOFs synthesized at different temperatures in a solvent ratio of DIW: Et = 2: 3, (a-e) are 23 h, 26 h, 29 h, 32 h and 35 h, respectively.
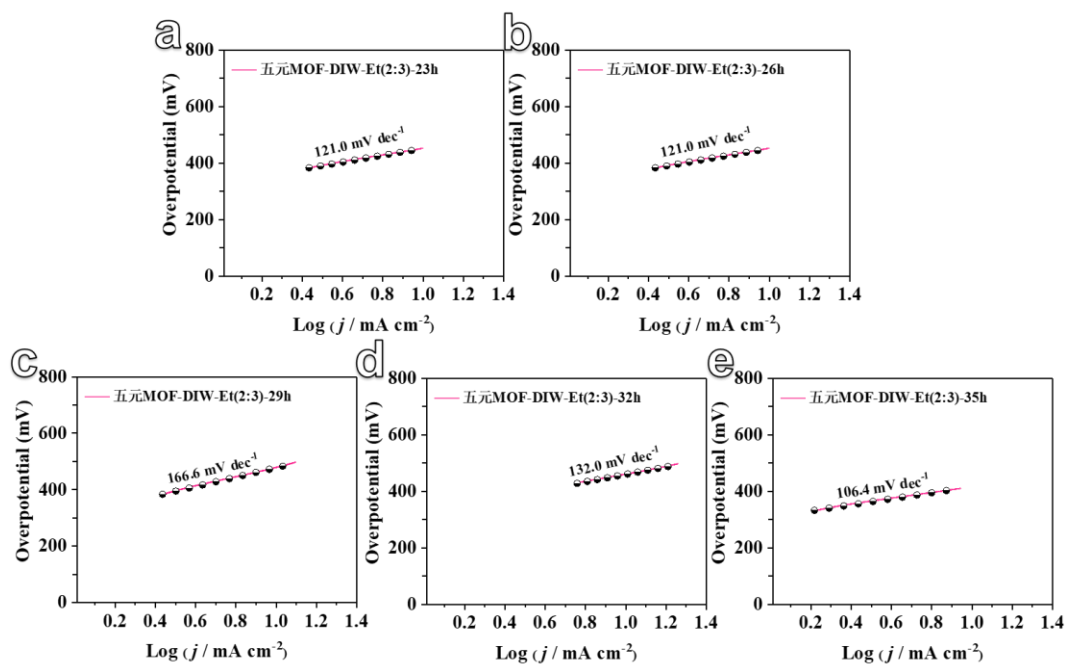
Figure S30. Tafel slope plots of MOFs synthesized at different temperatures in a solvent ratio of DIW: Et = 3: 2, (a-e) are 23 h, 26 h, 29 h, 32 h and 35 h, respectively.

Figure S31. Tafel slope plots of MOFs synthesized at different temperatures in a solvent ratio of DIW: Et = 4: 1, (a-e) are 23 h, 26 h, 29 h, 32 h and 35 h, respectively.

Figure S32. Tafel slope plots of MOFs synthesized at different temperatures in a solvent ratio of DIW: Et = 5: 0, (a-e) are 23 h, 26 h, 29 h, 32 h and 35 h, respectively.
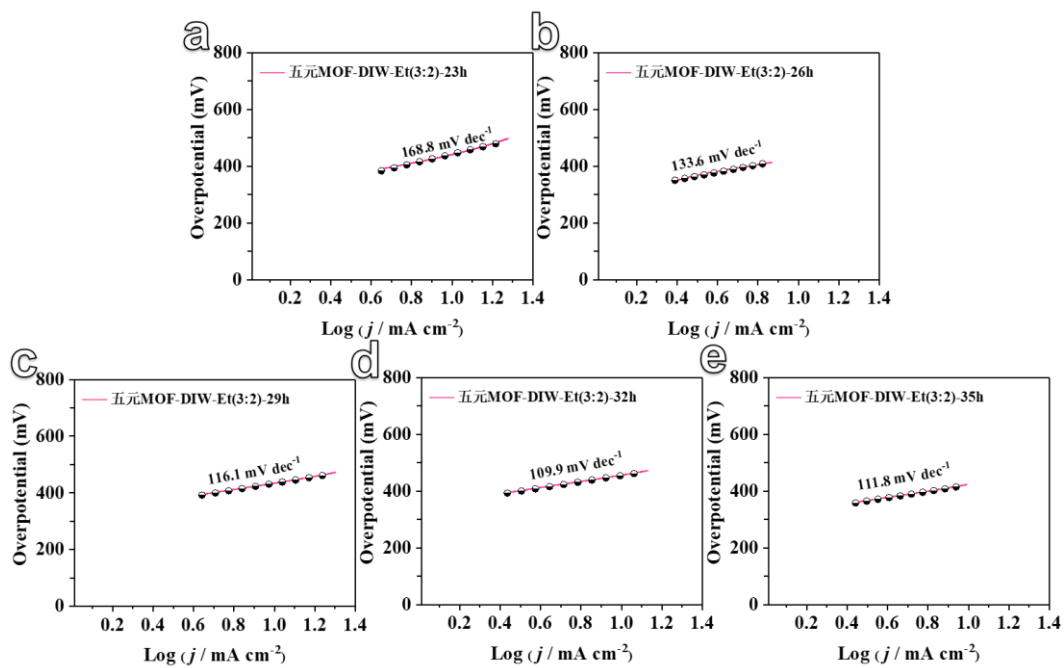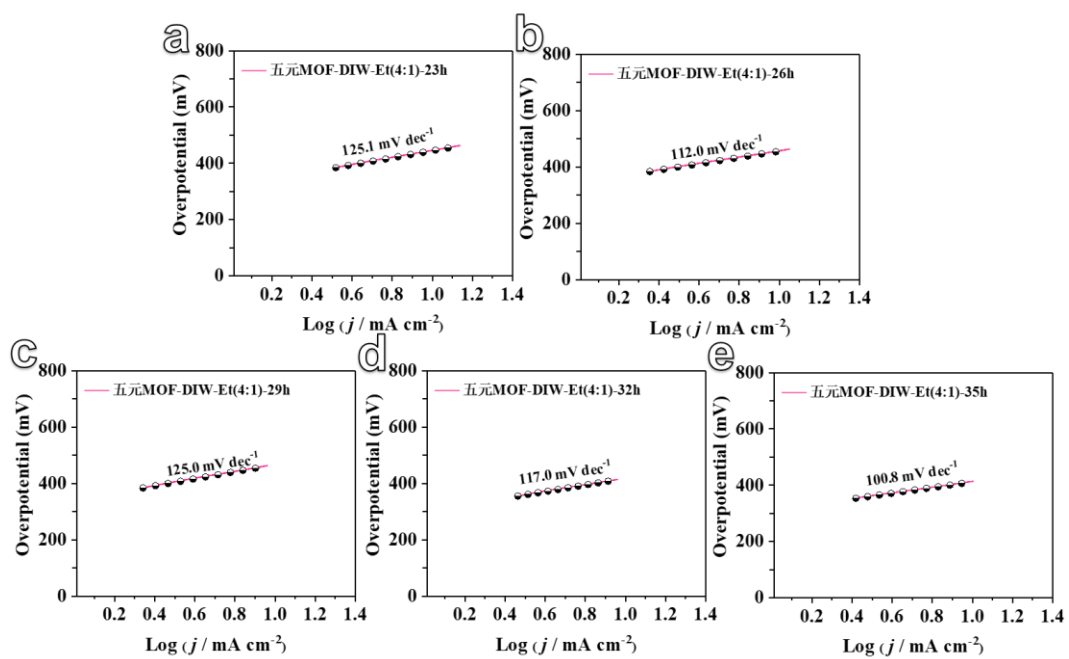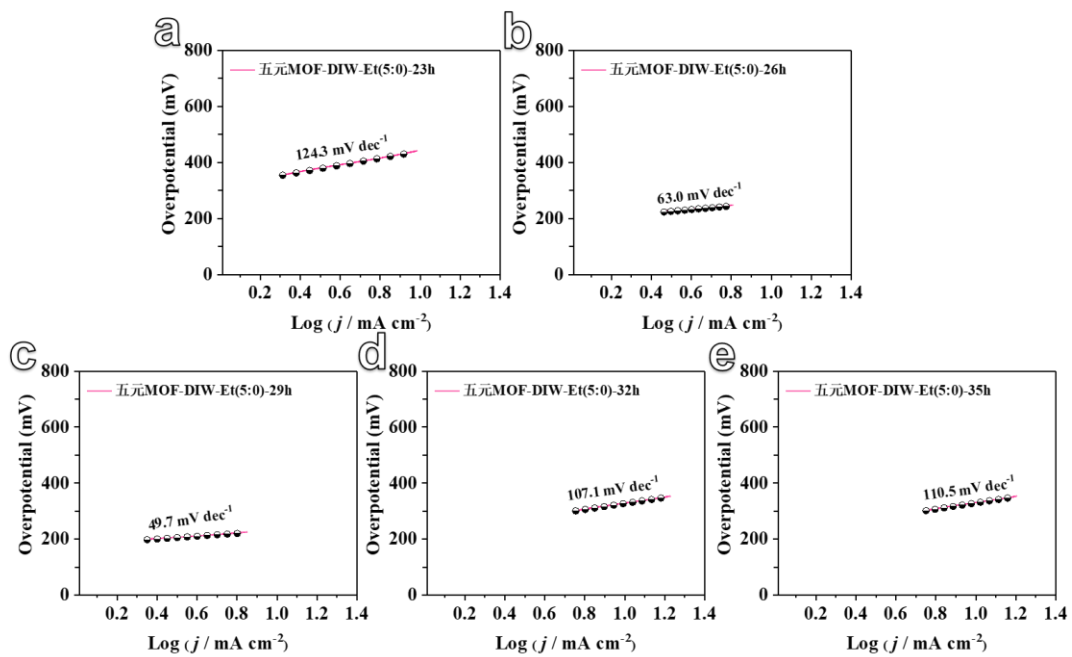
Table S2. Comparison of the OER activity for the five-metal MOF (GBR) with

several recently reported highly active electrocatalysts.

Catalyst	η_{10}(mV)	Tafel slope (mV dec^{-1})	Reference
five-metal MOF	306	133.6	This work
NiFe LDH	254	32	1
DH-CoFe LDHs	276	40.3	2
MIL-88-FeNi	290	49	3
NiFe LDHs-VFe	245	70	4
NiFe LDH-A50	308	50	5
PA-ZnFeCo LDH/NF	221	58.73	6
NiCo$_2$O$_4$ nanosheets	343	66	7
SC$_8$-NiCoLDH/CNO	290	31	8
NiFe-WO$_4$-LDH	290.3	41.6	9
NiFe-LDH (POM)	287	43	10

Supplemental References

1. Y. Zhao, X. Zhang, X. Jia, G. I. N. Waterhouse, R. Shi, X. Zhang, F. Zhan, Y. Tao, L.Z. Wu, C.H. Tung, D. O'Hare and T. Zhang, *Adv. Energy Mater.*, 2018, **8**, 1703585.

2. P. Zhou, J. He, Y. Zou, Y. Wang, C. Xie, R. Chen, S. Zang and S. Wang, *Science China Chemistry*, 2019, **62**, 1365-1370.

3. J.Y. Fu, Z.Y. Lin, J.Y. Xie, Y.M. Chai and B. Dong, *Materials Letters*, 2022, **324**, 132748.

4. Y. Wang, M. Qiao, Y. Li and S. Wang, *Small*, 2018, **14**, 1800136.

5. C. Peng, N. Ran, G. Wan, W. Zhao, Z. Kuang, Z. Lu, C. Sun, J. Liu, L. Wang and H. Chen, *ChemSusChem*, 2020, **13**, 811-818.

6. J. Han, J. Zhang, T. Wang, Q. Xiong, W. Wang, L. Cao and B. Dong, *ACS Sustain. Chem. Eng.*, 2019, **7**, 13105-13114.

7. S. Wang, T. Wang, X. Wang, Q. Deng, J. Yang, Y. Mao and G. Wang, *Int. J. Hydrogen Energy*, 2020, **45**, 12629-12640.

8. B.J. Waghmode, A.P. Gaikwad, C.V. Rode, S.D. Sathaye, K.R. Patil, D.D. Malkhede, *ACS Sustain. Chem. Eng.*, 2018, **6**, 9649-9660.

9. X. Xue, F. Yu, B. Peng, G. Wang, Y. Lv, L. Chen, Y. Yao, B. Dai, Y. Shi and X. Guo, *Sustainable Energy & Fuels*, 2019, **3**, 237-244.

10. X. Xue, F. Yu, J.G. Li, G. Bai, H. Yuan, J. Hou, B. Peng, L. Chen, M.F. Yuen, G. Wang, F. Wang, C. Wang, *Int. J. Hydrogen Energy*, 2020, **45**, 1802-1809.